Incorporating Temporary Coherent Scatterers in Multi-Temporal InSAR Using Adaptive Temporal Subsets

Hu, Fengming; Wu, Jicang; Chang, Ling; Hanssen, Ramon

DOI
10.1109/TGRS.2019.2915658

Publication date
2019

Document Version
Accepted author manuscript

Published in
IEEE Transactions on Geoscience and Remote Sensing

Citation (APA)
Hu, F., Wu, J., Chang, L., & Hanssen, R. (2019). Incorporating Temporary Coherent Scatterers in Multi-Temporal InSAR Using Adaptive Temporal Subsets. *IEEE Transactions on Geoscience and Remote Sensing*, *57*(10), 7658-7670. Article 8756305. https://doi.org/10.1109/TGRS.2019.2915658

Incorporating Temporary Coherent Scatterers in Multi-temporal InSAR Using Adaptive Temporal Subsets

Fengming Hu, Jicang Wu, Ling Chang and Ramon F. Hanssen, *Senior Member, IEEE*

***Abstract*—Multi-temporal interferometric synthetic aperture radar (MT-InSAR) is used for many applications in earth observation. Most MT-InSAR methods select scatterers with high coherence throughout the entire time series. However, as time series lengthen, inevitable changes in surface scattering lead to decorrelation, which systematically decreases the number of coherent scatterers. Here we propose a novel method to detect and process temporary coherent scatterers (TCS) by subsequently analyzing the amplitude and the interferometric phase. Two hypothesis tests are developed for amplitude analysis in order to identify the moments of appearing and/or disappearing coherent scatterers. Based on the amplitude analysis, the parameters of interest are then estimated using the interferometric phase. An optimized adaptive temporal subset approach is proposed to improve the precision of the estimated parameters. If the scatterers are not evenly distributed over the area, a secondary (support) network is designed to improve the spatial point distribution. The main advantage of this method is the reliable extraction of a subset of time series without using any contextual information. Experimental results show that the TCSs significantly increase the number of observations for displacement monitoring, and improve the change detection capability in urban construction areas.**

***Index Terms*—Temporary coherent scatterer, multi-temporal InSAR, change detection, Rayleigh distribution**

I. Introduction

DIFFERENTIAL Interferometric Synthetic Aperture Radar (DInSAR) is able to monitor the displacements of geo-objects with millimeter-level accuracy. However, this accuracy is significantly reduced due to atmospheric delays and decorrelation noise [1], [2]. To overcome this limitation, multi-temporal InSAR (MT-InSAR) has become the standard approach to detect subtle deformations. There are three types of methods for MT-InSAR. First, the Small BAseline Subset (SBAS) method is used in geodetic applications over wide scales [3], [4], [5]. This method requires groups of contiguous scatterers to be coherent [6] over limited temporal and spatial baseline ranges. Effectively, the process of multi-looking is applied to improve the correlation at the expense of a loss of resolution [7].

The second type of methods is based on point (persistent) scatterers (PS) and/or distributed scatterers (DS). PS-InSAR [8], [9] focuses on point, or single scatterers with high coherence during the whole acquired time. The PS can be selected either by the normalized amplitude dispersion (NAD) [9] or by the Signal-to-Clutter Ratio (SCR) [10]. This method overcomes the limitation of decorrelation due to spatial and temporal baselines and works well especially in urban areas, as lots of PS targets, related to man-made objects, can be found there [11], [12], [13]. However, it has limited applicability in rural areas. Compared to PS, DS decorrelate temporally and typically span several pixels where the amplitude is small but statistically homogeneous , which is common in rural areas. The phase of DS is obtained by using all combinations of interferograms [14], [15] to avoid temporal decorrelation.

Hybrid methods form the third type of MT-InSAR approaches. Here, high coherence scatterers are selected based on other criteria, such as coherence[16], phase analysis [17], [18], maximum likelihood estimation[19], or eigenvalues of the coherence matrix[20], which include not only PS but also high quality DS.

In most methods, selected points are expected to maintain high coherence over the entire time series. However, for longer time series SAR data, pixels may exhibit PS behavior only during parts of the time series, here referred to as temporary coherent scatterers (TCS) [21], [22], [23]. In [21], an abrupt change is detected using a Bayesian step detector considering a gaussian approximation for the amplitude. In [22], an analysis of phase and amplitude is performed to detect TCS, and a TCS start and stop time is estimated from the amplitude data, using a genetic algorithm. In [23], [24], TCS are selected by assuming amplitude stability over consecutive SAR image pairs and evaluated using a multi-master interferogram stack. Detecting a significant change in the time series of a single pixel is the main problem in selecting TCS. Compared to the interferometric phase, the amplitude is considered to be strongly related to the property of ground targets [25], [26]. Detecting a temporal change in the amplitude time series of a single pixel was performed using ANOVA (analysis of variance) by [27]. However, the hypothesis test of ANOVA assumes a Gaussian distribution [28], while the amplitude distribution may not be Gaussian. In fact, DS are often

This research was supported in part by the China Scholarship Council (201706260149), by the State Key Development Program for Basic Research of China (No.2013CB733304) and by the National Nature Science Foundation of China (No.41674003).

F. Hu is with the College of Surveying and Geo-Informatics, Tongji University, Siping Road 1239, Shanghai, 200092, China, and also with the Department of Geoscience and Remote Sensing, Delft University of Technology, Delft, 2628 CN, the Netherlands (email: f.hu-2@tudelft.nl).

R.F. Hanssen is with the Department of Geoscience and Remote Sensing, Delft University of Technology, Delft, 2628 CN, the Netherlands (email: r.f.hanssen@tudelft.nl).

J. Wu is with the College of Surveying and Geo-Informatics, Tongji University, Siping Road 1239, Shanghai, 200092, China.

L. Chang is with ITC, University of Twente, The Netherlands.

assumed to follow a Rayleigh distribution [25] while PS follow the Rice distribution [29].

The stability of the amplitude can be expressed by the normalized amplitude dispersion (NAD), where a low NAD, typically less than 0.25, is associated with a stable, strong scatterer. Selecting only points with a low NAD over the entire time series results in a spatially sparse data set with high quality, while increasing the NAD results in a more spatially dense dataset, albeit with variable quality. Therefore, different strategies are required depending on the quality of the selected points and the desired point density. For this reason, [30], [31] applied two consecutive networks (primary and secondary) with NAD thresholds of 0.25 and 0.45, respectively, to firstly detect potential high-quality points, followed by a densification to include more points. Similarly, [32] showed that the percentage of (phase) coherent points decreases rapidly with increasing NAD, and points with NAD > 1 should be treated as pure noise. However, for TCS, it is expected that the NADs of the entire time span can be much larger than one. More importantly, should TCS with a large NAD be erroneously selected as PS candidates, parts of the interferometric phases will be invalid, which will bias the estimated parameters.

Here, we present an optimal way for jointly modelling of TCS and PS using both amplitude and interferometric phase time series. First, we briefly introduce the statistical characteristics of the amplitude time series of a single pixel and establish a change detection algorithm using two hypothesis tests based on the Rayleigh distribution. TCS are selected only for coherent subsets of the time series and step-times are identified automatically. Then the process of MT-InSAR combining TCS and PS is reviewed including arc solution, network construction, parameter estimation and precision assessment. Additionally, an adaptive temporal subset approach based on the length of the time series and a secondary network is adapted to the interferometric process. Finally, we apply our method to real SAR data. Both single pixel change detection and interferometric processing are compared with conventional methods.

This paper is organized as follows. We introduce the amplitude process in selecting TCS, Section II, followed by the interferometric phase processing, Section III. Two real data results are presented in Section IV, followed by the conclusions in Section V.

II. Amplitude analysis

A. Statistical Characteristics of Amplitude

The observation of every single pixel in a SAR image is the summation of all elementary scatterers within a resolution cell, which is defined as a complex Gaussian random variable with variance σ^2 [1], [33]. The complex number Z is usually expressed as

$$Z = A \cdot e^{-j\psi}, \tag{1}$$

where A and ψ represent the amplitude and phase, with a joint probability density function (PDF) defined as

$$f(Z) = \frac{1}{2\pi\sigma^2} \exp\left(-\frac{\mathrm{Re}(Z)^2 + \mathrm{Im}(Z)^2}{2\sigma^2}\right). \tag{2}$$

TABLE I: Taxonomy of classes of scatterers based on coherence, including their acronyms, amplitude PDF's and expected normalized amplitude dispersion (NAD)

	Cont.Coh	Temp.Coh	Incoh.
Distr.Scat	**CCDS**	**TCDS**	**IDS**
	Rice (low SNR)	Rice (low SNR) & Rayleigh	Rayleigh,
	NAD low	NAD high	NAD medium
Point.Scat	**CCPS**	**TCPS**	unlikely
	Rice (high SNR), [29]	Rice (high SNR) & Rayleigh	
	NAD lowest	NAD highest	
	CCS	**TCS**	

Considering the property of the scatterers, it ranges from point scatterers to distributed scatterers [1]. A scatterer is considered to be 'coherent' to some degree, if the physical scattering mechanism does not change significantly over a given time interval. Based on the coherence, we distinguish three classes, (i) incoherent scatterers, where the coherence drops significantly within the repeat-interval of the satellite, (ii) continuously (persistently) coherent scatterers, i.e., coherent over the entire time interval, and (iii) temporary coherent scatterers (TCS), where coherence is only occurring over a subset of the entire time series see TABLE I. According to this taxonomy, the associated amplitude time series can be divided into five classes, as shown in TABLE I. The PDF of the amplitude holds information of the class of scatterers we are dealing with.

For incoherent distributed scatterers (IDS), we assume that the amplitude A follows a Rayleigh distribution [25], which is a special case of the Rice distribution [34]. This follows from the joint PDF in (2), see [1], with a PDF defined as

$$f(A|\sigma) = \frac{A}{\sigma^2} e^{-\frac{A^2}{2\sigma^2}}, \quad A \geq 0, \tag{3}$$

where σ^2 is the variance of the signal, here estimated per point over time. Its cumulative distribution function (CDF) is given as

$$F(A|\sigma) = 1 - e^{-\frac{A^2}{2\sigma^2}}, \; A \geq 0. \tag{4}$$

If A_i, with $i \in [1, m]$ are m independent observations from a Rayleigh distribution, the unbiased estimator of σ^2 is [35], [36]

$$\hat{\sigma}^2 = \frac{1}{2m} \sum_{i=1}^{m} A_i^2. \tag{5}$$

The amplitude of continuously coherent point scatterers (CCPS) follows a Rice distribution [29] with a high signal to noise ratio (SNR) while that of continuously coherent distributed scatterers (CCDS) follows a Rice distribution with low SNR. In the following discussion, there is no need to distinguish point or distributed scatterers. For this reason, we will refer to continuously coherent scatterers (CCS) and temporary coherent scatterers (TCS) from now on, see TABLE I. However, as the treatment of continuously coherent scatterers is stated in conventional PS-InSAR processing, this is not further considered here. We assume that TCS are characterized by a change from Rice to Rayleigh, or vice

versa. The basic rationale underlying our assumption is that a coherent DS will show less variability in its amplitude (over time) than an incoherent DS. This follows from the assumption that an incoherent DS can only be incoherent if it experiences changes over time. This difference in amplitude behavior for both categories of DS should therefore result in different distributions. The Rice distribution is a generic distribution, with two extremes. On one hand, if the amplitude is relatively high and stable, this is expressed in a high non-centrality parameter, which means that the Rice distribution will be more Gaussian-like. That is, it will be less likely that (during the time series) amplitudes can occur which are either much higher, or much lower than the mean. On the other hand, if the amplitude is varying more (as a consequence of temporal decorrelation), which means that there is a higher likelihood for both higher as well as lower amplitudes, the Rice distribution is more Rayleigh-like. This follows from the fact that the Rayleigh distribution has a longer tail for higher amplitudes, while the amplitudes lower than the mean are less unlikely.

B. TCS Candidates

Considering the NADs of different scatterers, CCS have the smallest values, IDS medium, while the TCS have the greatest values. Therefore, It is more likely to mis-classify an IDS as being a TCS. Moreover, the number of IDS is much larger than that of other scatterers. Therefore, removing most IDS from the TCS candidates will reduce the mis-classifications and improve the efficiency.

We perform a hypothesis test (here referred to as Rayleigh Test) to test whether m observations stem from the same Rayleigh distribution[35].

First, we estimate the variance σ^2 using (5). Then, we reorder the observations (amplitudes), which have the range $(0,\infty)$, in increasing order and bin them into B bins $(0,x_1),(x_1,x_2),\cdots,(x_{B-1},\infty)$ with varying bin-widths, but constant probability. [36] recommends B to be at least 5. We compute the upper boundary, x_i of the ith bin using (4) under the condition that the expected number of observations in each bin is equal, i.e., m/B. Adapting (4) to

$$P(0 \le x < x_i) = 1 - e^{-\frac{x_i^2}{2\sigma^2}} = \frac{i}{B}, \;\; i = 1,\ldots,B-1, \quad (6)$$

we invert this to obtain the upper boundary x_i:

$$x_i = \sqrt{2\sigma^2 \ln\left(\frac{B}{B-i}\right)}, \;\; i = 1,\ldots,B-1. \quad (7)$$

Supposing that the total number of observations in the ith bin is f_i, the test statistic is defined as [36]

$$\chi_0^2 = \sum_{i=1}^{B} \frac{(f_i - m/B)^2}{m/B}, \quad (8)$$

where χ_0^2 follows a χ^2 distribution with $B-2$ degrees of freedom [37]. Given the significance level α, the critical value χ_α^2 is obtained. If $\chi_0^2 < \chi_\alpha^2$, we sustain the hypothesis that the m observations are from the same distribution, which means the pixel did not change during the acquisition time, hence it is not a temporary coherent scatterer. Note that due to speckle noise in the single look image, increasing the significance level α will lead to more detected changes, hence more potential TCS's. This initial result will be refined in the following steps.

C. Step-change Location Estimation (Heaviside function)

Determining for which period a point is coherent requires locating the time of a step-wise change automatically. We propose an iterative algorithm under the assumption that the two subsets of amplitude time series on each side of the step are from different distributions if a change happens to the ground targets and this step is applied on the TCS candidates obtained in Section II-B. This problem is tackled via another hypothesis test: testing whether the two independent subsets are from the same Rayleigh distribution. First, we consider the single-step case. If this step is located between the pth image and the $p+1$th image, the whole time series is divided into two groups, $A_1,\ldots,A_p$ and $A_{p+1},\ldots,A_m$. To test the hypothesis that $\sigma_1^2 = \sigma_2^2$, the test statistic is defined as [36]

$$F_p = \frac{\sum_{i=1}^{p} A_i^2}{2p} \Big/ \frac{\sum_{i=p+1}^{m} A_i^2}{2(m-p)} = \frac{\hat{\sigma}_1^2}{\hat{\sigma}_2^2} \sim F_{2p,2(m-p),0}, \quad (9)$$

with a central F-distribution with $2p$ and $2m-2p$ degrees of freedom, where $\hat{\sigma}_1^2$ and $\hat{\sigma}_2^2$ denote the unbiased estimated variances of the two subsets. Its worth noting that the F-value is always larger than one. The ratio and degrees of freedom are inverted when $\hat{\sigma}_1^2 < \hat{\sigma}_2^2$. Given the significance level α, the critical value F_α is obtained. If $F_p > F_\alpha$, we reject the hypothesis that the two subsets are from the same distribution, which means that the step is located after the pth image. At this time, decreasing the significance level α will reduce the number of false detected TCS. This way, the location of the step is given by

$$\hat{p} = \arg\max_{p=1:m-1} \left(\frac{\sum_{i=1}^{p} A_i^2}{2p} \Big/ \frac{\sum_{i=p+1}^{m} A_i^2}{2(m-p)} \right). \quad (10)$$

If more than one step exists, this process can be repeated several times until no step exists in the remaining subsets of the time series. Based on the above two hypothesis tests (8) and (9), the whole approach of identifying TCS is established, which is shown in Fig. 1. This yields a time series which is divided into $n+1$ subsets with n step-times. The MT-InSAR process requires enough observations in time domain, as the number of images must be larger than a particular threshold [9]. The IDS among the TCS candidates will have an F_p values smaller than the F_α, and will be removed in this process. Additionally, CCS are removed based on the PS-InSAR result.

This approach allows us to distinguish three possible changes, (i) "appearing" TCS: the time series is coherent from the last step-time to the end, (ii) "disappearing" TCS: the time series is coherent from the first acquisition up to the first step-time, and (iii) "visiting" TCS: the time series is coherent between two adjacent step-times (at least two step-times exist in this case).

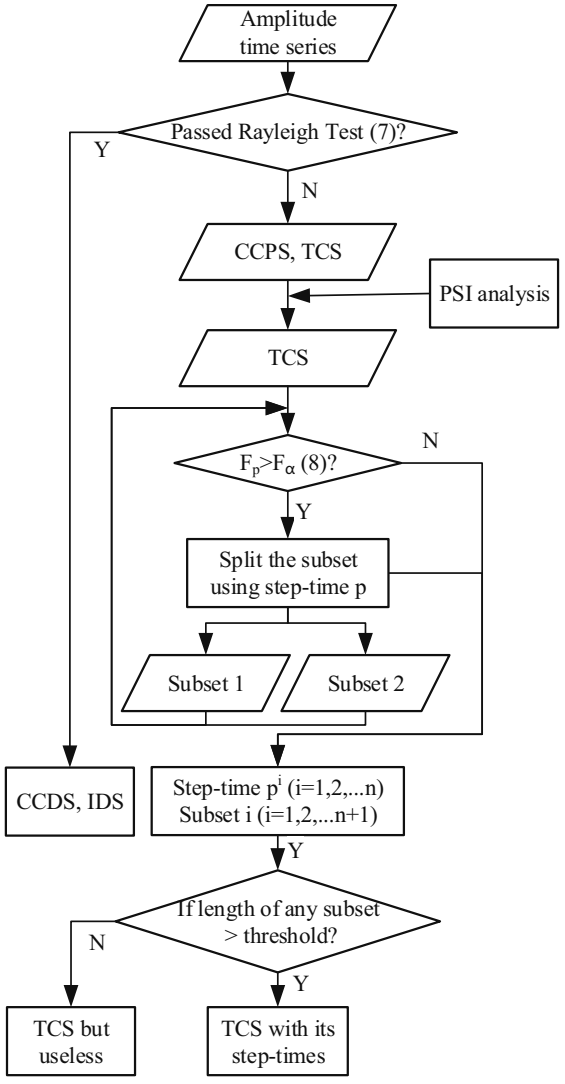

Fig. 1: Flowchart of iteratively identifying TCS. This procedure is part of the total flow chart in Fig. 2.

III. Phase analysis

A. Arc Solution

In MT-InSAR, the basic observations are the differential interferometric phases of the arcs. Considering $m-1$ differential interferograms from m SAR images, the phase difference between two points i and j of a single arc in the kth interferogram can be expressed as follows:

$$\Delta\phi_{i,j}^{k} = C_{i,j} - \frac{4\pi}{\lambda}\frac{B_{\perp,i}^{k}}{R_i \sin\theta_i}\Delta h_{i,j} - \frac{4\pi}{\lambda}t^{k}\Delta v_{i,j} + 2\pi n_{i,j}^{k} + e_{i,j}^{k}, \tag{11}$$

where $\Delta h_{i,j}$ and $\Delta v_{i,j}$ denote the residual height difference and the velocity difference between the two points; $n_{i,j}^{k} \in \mathbb{Z}$ denotes the integer phase ambiguity; t^{k} and $B_{\perp,i}^{k}$ denote the temporal baseline and perpendicular baseline respectively; R_i is the slant range, θ_i is the local incidence angle and λ is the radar wavelength; $C_{i,j}$ denotes the phase constant that corresponds to the atmospheric delay difference in the master image, and $e_{i,j}^{k}$ denotes the random error of the phase, including the atmospheric delay difference in the slave image. The Integer Least Squares (ILS) model of PS can be defined as follows [38]:

$$\begin{aligned} E\{\begin{bmatrix} \Delta\phi_{i,j}^{1} \\ \vdots \\ \Delta\phi_{i,j}^{m-1} \end{bmatrix}\} &= \begin{bmatrix} 2\pi & 0 & 0 \\ 0 & \ddots & 0 \\ 0 & 0 & 2\pi \end{bmatrix} \begin{bmatrix} n_{i,j}^{1} \\ \vdots \\ n_{i,j}^{m-1} \end{bmatrix} \\ &\quad - \frac{4\pi}{\lambda}\begin{bmatrix} \frac{B_{\perp,i}^{1}}{R_i \sin\theta_i} & t^{1} \\ \vdots & \vdots \\ \frac{B_{\perp,i}^{m-1}}{R_i \sin\theta_i} & t^{m-1} \end{bmatrix} \begin{bmatrix} \Delta h_{i,j} \\ \Delta v_{i,j} \end{bmatrix} + C_{i,j}, \end{aligned} \tag{12}$$

where $E\{\cdot\}$ denotes the expectation. Arc solutions are obtained using (12), and details of the main process can be found in [39]. In our approach, the variance-covariance (VC) matrix used to weight the observations is determined by variance component estimation (VCE). Phase unwrapping for arcs is implemented using the Lambda method [38], [40] and the validation of the ambiguity resolution is tested by the ratio test [41]. Then parameters can be estimated using a least-squares approach, satisfying the acceptance condition.

Then the model for appearing TCS, disappearing TCS, and visiting TCS is defined as:

$$\begin{aligned} E\{\begin{bmatrix} \Delta\phi_{i,j}^{t_{\text{start}}} \\ \vdots \\ \Delta\phi_{i,j}^{t_{\text{stop}}} \end{bmatrix}\} &= \begin{bmatrix} 2\pi & 0 & 0 \\ 0 & \ddots & 0 \\ 0 & 0 & 2\pi \end{bmatrix} \begin{bmatrix} n_{i,j}^{t_{\text{start}}} \\ \vdots \\ n_{i,j}^{t_{\text{stop}}} \end{bmatrix} \\ &\quad - \frac{4\pi}{\lambda}\begin{bmatrix} \frac{B_{\perp,i}^{t_{\text{start}}}}{R_i \sin\theta_i} & t_{\text{start}} \\ \vdots & \vdots \\ \frac{B_{\perp,i}^{t_{\text{stop}}}}{R_i \sin\theta_i} & t_{\text{stop}} \end{bmatrix} \begin{bmatrix} \Delta h_{i,j} \\ \Delta v_{i,j} \end{bmatrix} + C_{i,j}, \end{aligned} \tag{13}$$

where t_{start} and t_{stop} denote the locations of the step-times as discussed in Section II-C. For appearing TCS, t_{stop} is $m-1$ and t_{start} is the last step-time. For disappearing TCS, t_{stop} is the first step-time and t_{start} is 1. For visiting TCS, t_{start} and t_{stop} are two adjacent step-times.

B. Network Construction

As TCS and PS time series have different lengths, it is not possible to process them together. Additionally, PS selected by different thresholds will also have a different noise level. Therefore, an agile processing method is required and points with different qualities should be processed with different strategies. Fig. 2 shows the flowchart of processing points in different groups. During our processing, points are divided into three groups, (i) PS with low noise, (ii) PS with medium noise and (iii) TCS. These three groups are processed separately.

First, PS points with low noise are selected with a strict threshold to provide high precision of the final result. For example, 0.25 is a recommended threshold of the normalized amplitude dispersion (NAD) to select PS [9]. In this group, VCE is applied to determine the weight matrix and parameters for the orbit error are estimated if necessary. Then the reference network is established using two steps. An initial network is generated by a Delaunay network to link all points. After

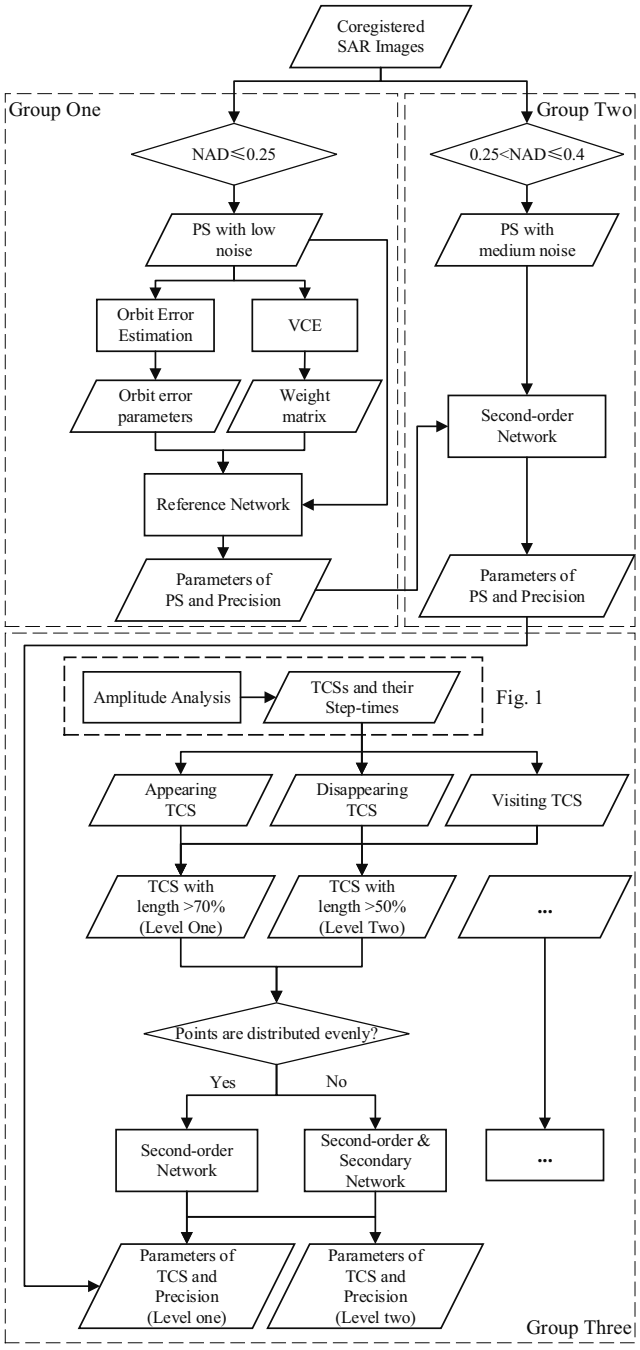

Fig. 2: Flowchart of processing points in different groups.

removing poor arcs, the main network which contains most points is identified by the depth-first search algorithm [42]. Every isolated point is connected to its nearest neighbors in the main network and the number of nearest points is increased sequentially. Additionally, only points that are connected to other points more than two times are accepted in the reference network.

Second, points with medium noise are selected by increasing the NAD threshold . A second-order network is used to link these new points to the reference network. This process is similar to the second step in the reference network. New arcs are generated by connecting every point to its nearest neighbors in the reference network and these new arcs are solved using the same way. During this process, the weight matrix and the parameters of the orbit error, as determined by the reference network, are used again.

Third, TCS and their step-times are obtained by amplitude analysis. In the third group, the three types of TCS (appearing, disappearing and visiting TCS) are processed using the same way separately. First of all, TCS are divided into several levels of temporal subsets according to the subset length. Fig. 3 illustrates three levels of adaptive temporal subsets on 45 randomly selected TCS including 15 appearing TCS, 15 disappearing TCS and 15 visiting TCS. Then every TCS is connected to its nearest PS to generate the second-order network at each level. Unfortunately, if PS are unevenly distributed over the area, its difficult to find a sufficient number of arcs between TCS and PS. So a secondary network is adopted. The first network is used to link some of the TCS to the PS network and the secondary network is used to link remaining TCS to the previously linked TCS for each type of TCS separately. Here, we always connect "new" *appearing* TCS to previously linked *appearing* TCS since they always span a common time interval, cf. Fig. 3. This also holds for disappearing TCS. For visiting TCS, we calculate the length of the common time interval when connecting "new" visiting TCS to previously linked visiting TCS. If the length is smaller than a given threshold (see Fig. 2), this arc is dropped from the processing.

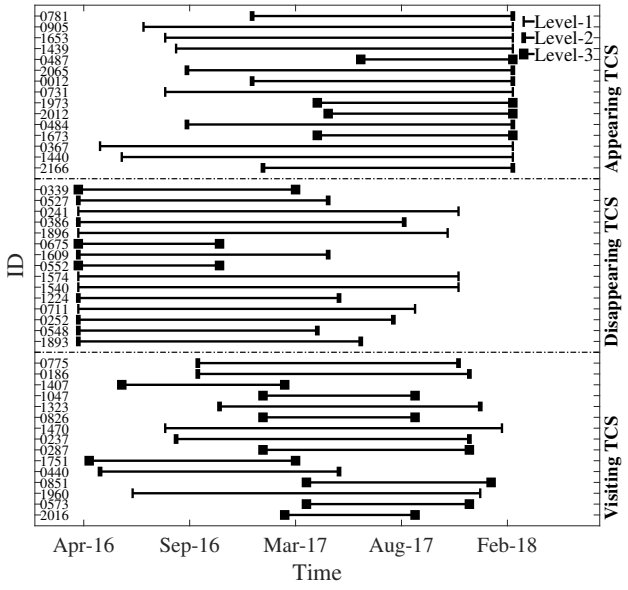

Fig. 3: Example of the adaptive temporal subsets on an arbitrary subset of TCS. Every point has its own coherence interval.

C. Parameter Estimation and Precision

In the reference network, a velocity map can be obtained for all n_1 points by integrating all arc solutions

$$v_1 = (B_1^T Q_1^{-1} B_1)^+ B_1^T Q_1^{-1} \Delta v_1, \tag{14}$$

where B_1 denotes the design matrix related to the network; Δv_1 denotes the estimated differential deformation rate of all arcs; $(\cdot)^+$ denotes the pseudo-inverse and is solved by a faster algorithm [43]. Q_1^{-1} is the weight matrix related to the quality of the arc solutions which is defined as

$$Q_1^{-1} = \text{diag}(\sigma_{\Delta v_1}^{-2}, \ldots, \sigma_{\Delta v_n}^{-2}), \tag{15}$$

where $\sigma_{\Delta v}^2$ denotes the variance of the estimated deformation rate and n denotes the number of accepted arcs. The term diag$(\cdot)$ denotes the diagonal elements of the matrix. The precision of all points can be estimated as follows:

$$D\{v_1\} = \sigma_1^2 (B_1^T Q_1^{-1} B_1)^+ (B_1^T Q_1^{-1} B_1)(B_1^T Q_1^{-1} B_1)^+, \tag{16}$$

where the σ_1^2 denotes the variance of unit weight. No reference point is specified during the estimation.

Based on the established reference network, PS points with medium noise as well as TCS can be included in the second-order network. The velocity map for n_2 new points can be obtained by integrating new arc solutions jointly with points in the reference (first-order) network. The estimated parameters of the points in the reference network don't change in the subsequent steps and the solution of the second-order network is formulated as follows:

$$\begin{bmatrix} v_2 \\ k \end{bmatrix} = \begin{bmatrix} B_2^T Q_2^{-1} B_2 & G^T \\ G & 0 \end{bmatrix}^{-1} \begin{bmatrix} B_2^T Q_2^{-1} \Delta v_2 \\ v_1 \end{bmatrix}, \tag{17}$$

where B_2 denotes the design matrix related to the network; Δv_2 denotes the estimated differential deformation rate of all arcs; Q_2^{-1} is the weight matrix related to the quality of the arc solution which is defined in the same way as Q_1^{-1}; and k is a Lagrange coefficient vector, without physical meaning which we don't use during the process.

The constraints matrix G is defined as:

$$G\, v_2 = v_1. \tag{18}$$

The first n_1 columns of matrix G are a unit matrix with dimension $n_1 \times n_1$, while the remaining n_2 columns are a zeros matrix with dimension $n_1 \times n_2$.

The precision of points in the second-order network can be formulated as follows:

$$D\{v_2\} = \sigma_2^2 (B_{22}^T Q_2^{-1} B_{22})^{-1} B_{22}^T Q_2^{-1} Q_l \cdot Q_2^{-1} B_{22} (B_{22}^T Q_2^{-1} B_{22})^{-1}, \tag{19}$$

where Q_l is defined as follows:

$$Q_l = Q_2 + B_{21}(D_{v_1}/\sigma_1^2) B_{21}^T, \tag{20}$$

where B_{21} and B_{22} are obtained by splitting the design matrix B_2:

$$B_2 = [B_{21}|B_{22}]. \tag{21}$$

IV. Experimental Results and Discussion

A. Change Detection of a Single Pixel

Real SAR data was used to test and demonstrate the change detection algorithm with amplitude time series of single pixels. All pixels are classified in three groups, based on their normalized amplitude dispersion (NAD). The first group, with NAD<0.25, is assumed to contain high quality PS points, which exhibit a homogeneous behavior over time. The second group, with 0.25 <NAD< 1 is assumed to contain PS points with more noise, as well as DS points. The third group, with NAD> 1 may hold points which are either incoherent, or exhibit a discontinuity in their temporal behavior (TCS).

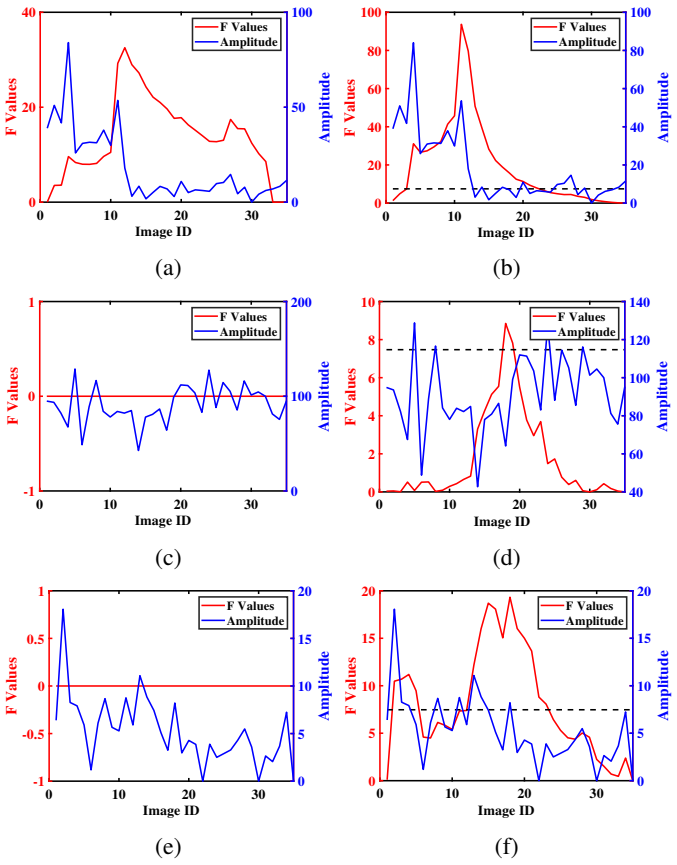

Fig. 4: Amplitude time series and F-values of three pixels. (a) (c) and (e) are the results of three time-series obtained by our method; (b) (d) and (f) are obtained by ANOVA. (the black dashed line indicates the threshold F-value.)

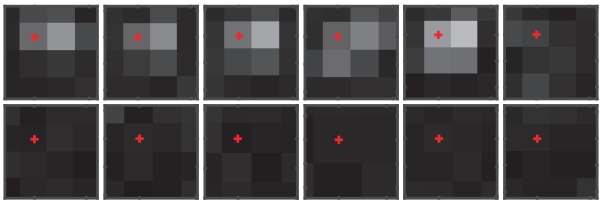

Fig. 5: Amplitude images of the first time series from the 7th to the 18th image.The first row corresponds to the amplitude images from the 7th to the 12th while the second row corresponds to the amplitude images from the 13th to the 18th. (Red cross indicates the location of the pixel.)

Three amplitude time-series from the different groups were chosen to validate our method, with NAD values of 1.04, 0.21 and 0.67, respectively. Setting the level of significance α to 0.02, both our method and ANOVA were applied to the three time series, see Fig. 4.

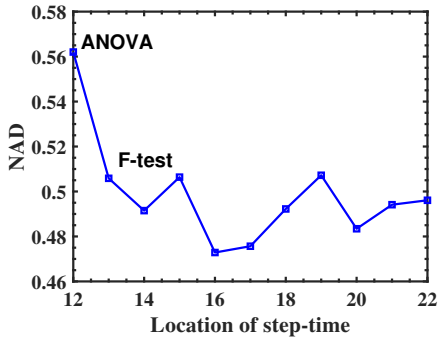

Fig. 6: NADs obtained by different positions of step-times using the first time series.

Figs. 4 (a), (c) and (e) are obtained by our method. Consecutively testing the step-time for each image, we obtain the corresponding F-values using (9). Different from ANOVA, the threshold of each F-value varies, so we set an F-value which is smaller than the critical value F_α to zero. The step-time is then located at maximum F-value. Here we only consider a single step-time. The step-time of the first time series is at the 12th image, while there are no changes in the second and third time series. Figs. 4 (b), (d) and (f) are obtained by ANOVA. The threshold for the F-value is represented as a black dashed line and the step-time is located at the maximum F-value, as long as it is also greater than the threshold. So the step-time of the first time series is after the 11th image and after the 18th and the 17th image, for the second and third time series, respectively. Then, we show the amplitude images of the first time series from the 7th to the 18th image in Fig. 5. The point changed from the 12th image, and there is no signal after the 12th image. Therefore, the step-time is located at the 12th image. Further, Fig. 6 shows the NADs obtained by different positions of step-times using the first time series. Comparing the positions of the step-times obtained by the two methods, the results by our method are more consistent with the actual situation.

While the algorithm indicates that there is no change (since $0.25 <$NAD< 1 for the third time series and NAD< 0.25 for the second time series), a visual inspection of the point confirms that the amplitude is very stable and the phase time series is steady-state. Therefore, the ANOVA method results in false alarms of changes.

On the other hand, considering the computational burden of single pixel change detection, time complexity of the two algorithms is compared. Supposing that only one step-time exists, the time complexity of both methods is $O(m)$. However, if there were s step-times, the time complexity of ANOVA is $O(m^s)$ while that of our method is $O(m \log m)$, which is much faster.

B. Case Study I: Delft

The first demonstration of the amplitude-augmented interferometric processing was implemented using forty Sentinel-1A (S1A) images between April 2016 and February 2018 in Delft, The Netherlands. The data set covered a 10×10 km area and was registered using GMT5SAR software [44]. The slant-range and azimuth pixel spacings are 2.3 m and 14.7 m, respectively.

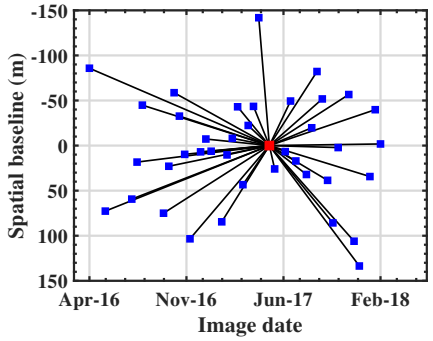

Fig. 7: Distributions of the temporal and spatial baselines. Red dot indicates the master image and blue dots indicate the slave images.

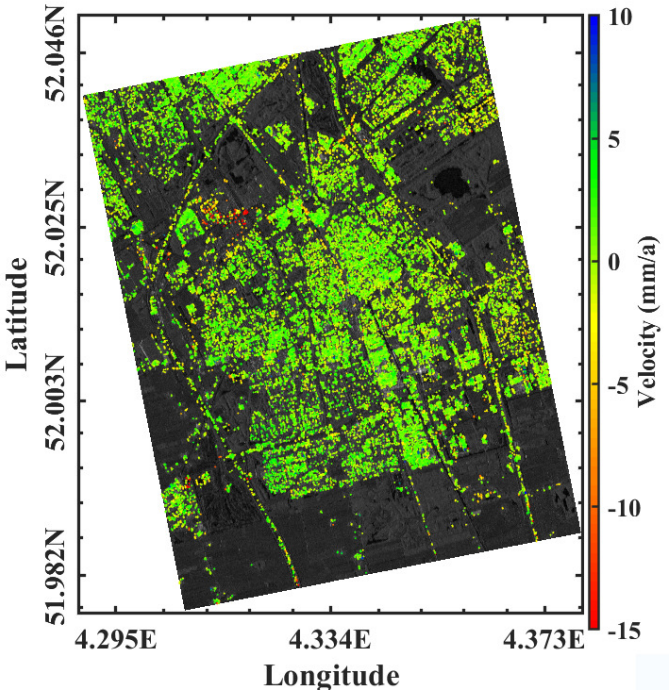

Fig. 8: Velocity on PSs in Delft, the Netherlands.

Most areas didn't change during the evaluated time slot and PS points were distributed with high density throughout the area. External digital elevation models (DEMs) were not used in our process and only a flattened phase correction was applied during data preprocessing. During the interferometric process, PS points in the first and second group were selected using an NAD with thresholds of 0.25 and 0.4. Higher values could be chosen as the second threshold, but the noise would increase accordingly. Fig. 7 shows the distribution of the spatial and temporal baselines. The maximum temporal baseline was 200 days and the maximum spatial baseline was less than 150 m.

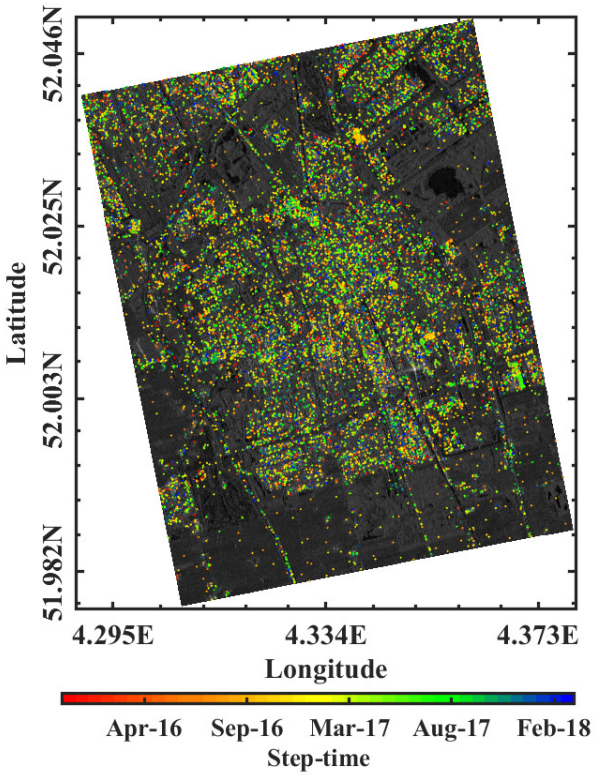

Fig. 9: Distribution of step-times on appearing TCS and disappearing TCS.

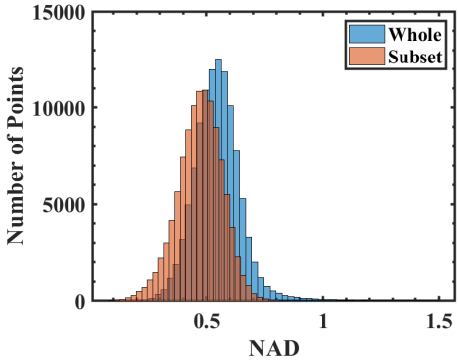

Fig. 10: Distribution of NADs on TCS obtained from the subset and the entire time series.

PS points in the first and second groups were solved and the final velocity map contained 50294 points, which is shown in Fig. 8. The subsidence rates range from -15 to $+10$ mm/a and PS points are evenly distributed over the whole area. Then the iterative change detection algorithm described in Section II was applied where the significance levels of the two hypothesis tests were set to 0.5 and 0.02. The initial result is extremely noisy, hence interferometric processing is required to refine the result. The distribution of the appearing and disappearing TCS with the corresponding step-times in the whole area are shown in Figs. 9. Based on the step-times, the NADs of the TCS can be recalculated using the subsets of the time series. Fig. 10 shows the distribution of the NADs on TCS by the entire and subset time series. If the threshold was set to 0.4, the number of available points increased from 6283 to 23273. Further, the longer the length of time series is, the higher the precision of the estimated parameters that can be obtained in the MT-InSAR algorithm. A temporal threshold on the subset length is set to obtain reliable solutions of TCS. In this case, the thresholds cover 70%, 50% and 30% of the whole time series, which corresponds to the length of 28, 20 and 12, respectively.

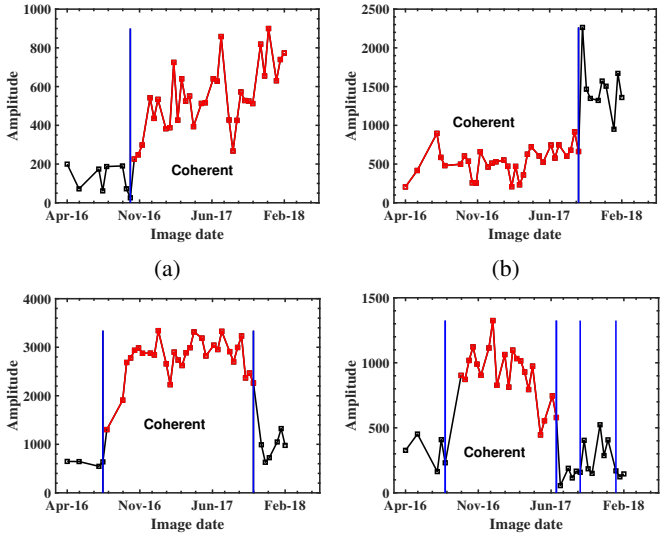

Fig. 11: Amplitude time series with adaptive temporal sampling on four TCS. Red lines indicates the coherent interval and blue lines mark the locations of step-times.

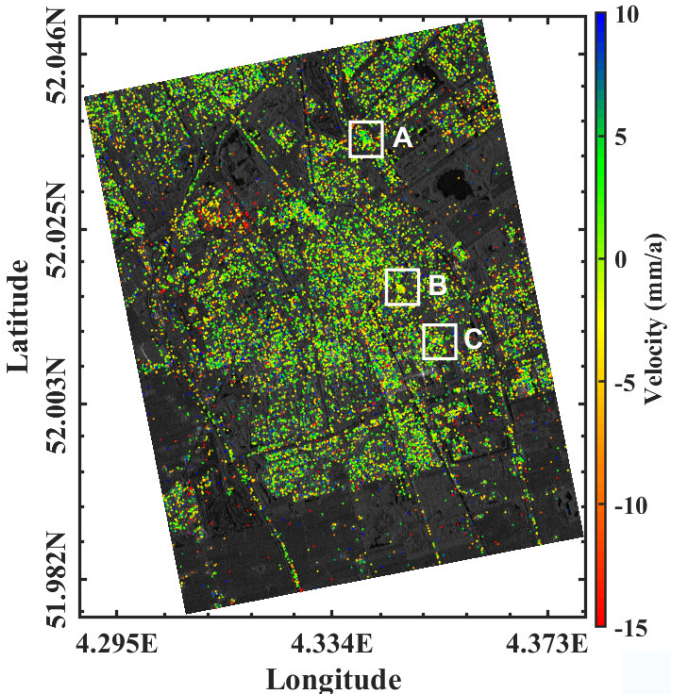

Fig. 12: Velocity on TCS in Delft. White rectangles identify the selected areas for details.

Four pixels are selected to show the amplitude time series with adaptive temporal subsets. Figs. 11 (a) and (b) are appearing and disappearing TCS. Figs. 11 (c) and (d) are visiting TCS. The coherent interval is determined by interferometric processing. Fig. 12 shows the velocity of the TCS. The number of accepted appearing TCS is 6741, that of the disappearing TCS is 7449 and that of the visiting TCS is 2188. We also estimate the standard deviations of linear deformation velocity for all TCS, which are used to evaluate the reliability of the parameters.

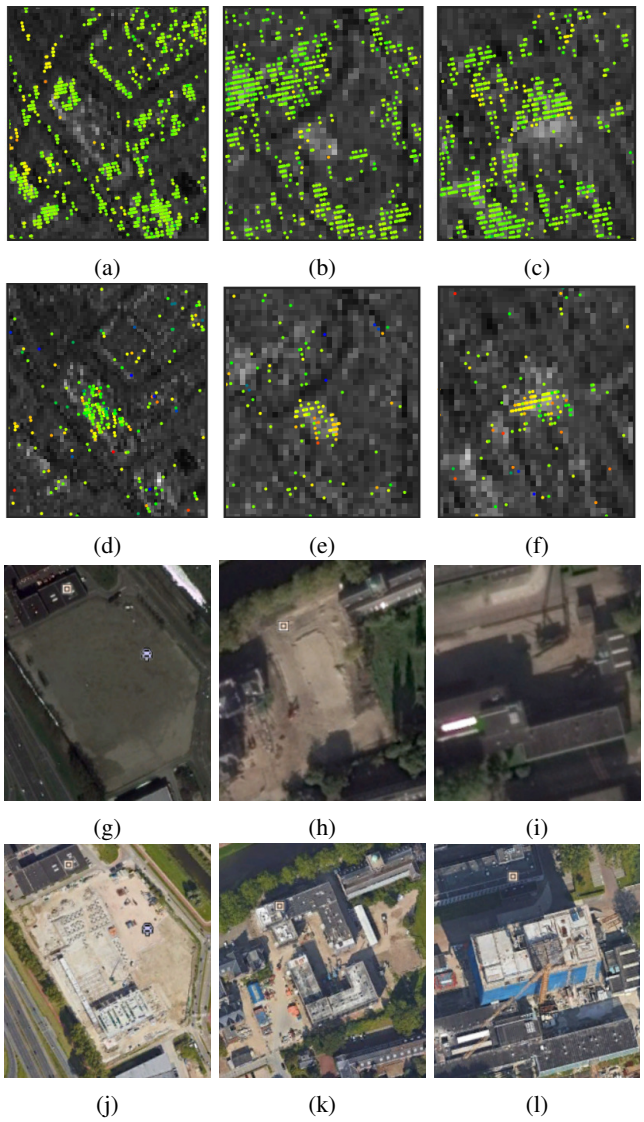

Fig. 13: Magnified views of selected area. The first row corresponds to velocity on PS, the second row to velocity on TCS, the third and the forth rows to Google Earth images. (a), (d), (g), and (j) are region A. (b), (e), (h), and (k) are region B. (c), (f), (i), and (l) are region C. Colors are as in Fig. 12.

Three small regions (A, B, and C) are selected to show more details, which are marked as three white rectangles in Fig. 12. There are new buildings in the three selected area and magnified views of these area are shown in Fig. 13. According to Figs. 13 (a)∼(f), results of PS do not include

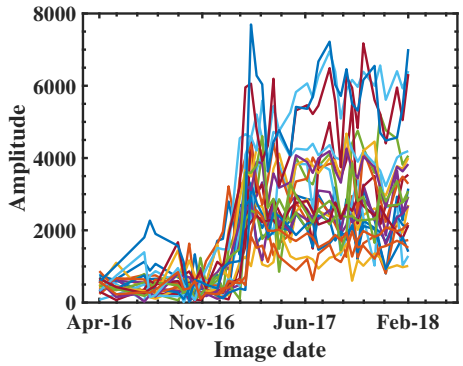

Fig. 14: Amplitude time series of the TCS in the area C.

any valid points in these areas, while results of TCS highlights these changes. Figs. 13 (g)∼(l) show the construction of the new buildings in the selected area from the Google Earth comparison, which shows good agreement with the result of TCS. It's obvious to find the changes caused by construction. Additionally, Fig. 14 shows the amplitude time series of several TCS in selected region B. All points contain a jump at similar times and their step-times are at the 9th, 10th and 11th image, which means this construction is most likely to occur between 16th January 2017 and 9th February 2017.

C. Case Study II: Shanghai HongQiao Airport

The second demonstration of the amplitude-augmented interferometric processing uses thirty-seven TerraSAR-X (TSX) images (Mar 2009–Oct 2012). The data set covered a 3×6 km area of Shanghai HongQiao international airport, during the time when the T2-terminal was built. The data set was coregistered using the GAMMA software. The slant-range and azimuth pixel spacing are 0.91 m and 1.97 m, respectively.

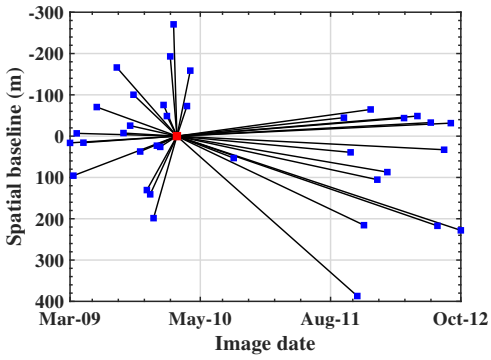

Fig. 15: Distribution of the temporal and spatial baselines. The red dot indicates the master image; blue dots indicate the slave images.

The thresholds and steps conducted in this case-study were identical to the ones in the Delft study area. The main difference between the two cases is the distribution of the points. Points in the Delft case are distributed with high density in the entire area, while points in the Shanghai case are distributed with high density only in some areas. Fig. 15 shows

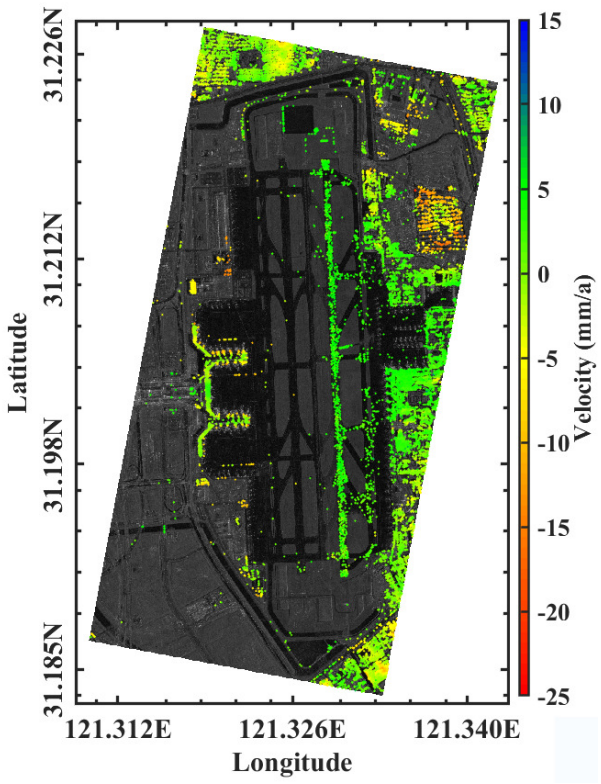

Fig. 16: Velocity on PS in Shanghai HongQiao airport.

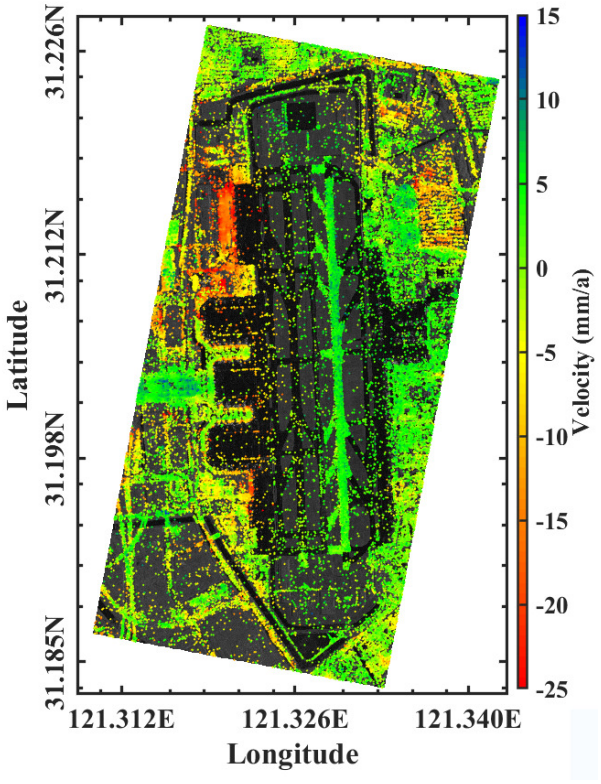

Fig. 17: Velocity on TCS in Shanghai HongQiao airport, visualized under the assumption that the velocity of each point is constant over the entire time range.

the distribution of the spatial and temporal baselines. The maximum temporal baseline was 850 days and the maximum spatial baseline was 400 m.

The final velocity map of PS contains 40934 points with subsidence rates ranging between -25 and $+15$ mm/a, see Fig. 16. PS points are only detected in the north and east area due to the construction of the airport during the entire (100%) time-range. Valid PS points are extremely sparse, so it is difficult to estimate the deformation of the entire area based on this result. If we plot appearing, disappearing, and visiting TCS in this area, we obtain Fig. 17, which contains 94519 points. Note that this is double the amount of PS, and therefore the inclusion of TCS to the PS yields an increase of 200% in the number of valuable points. Moreover, note that the visualization of these points in a single velocity figure is sub-optimal, as points which are coherent only over a subset of time may exhibit a different velocity compared to the continuously coherent PS points.

Comparison with the PS velocity map, cf. Fig. 16, shows buildings and constructions that were not detected using the full time series.

In addition to the TCS velocity map, the results of the amplitude-based change detection approach show the dates of appearance and disappearance of structures see Fig. 18. From the appearance map (left) in Fig. 18, the T2-terminal including its surrounding facilities and new roads around the airport were completed later than March 2011. According to the disappearance map (right), Fig. 18, some structures on the west of the airport were removed between Dec 2009 and Aug 2010. The homogeneity in the appearance and disappearance dates can be used as a reliability metric of the results.

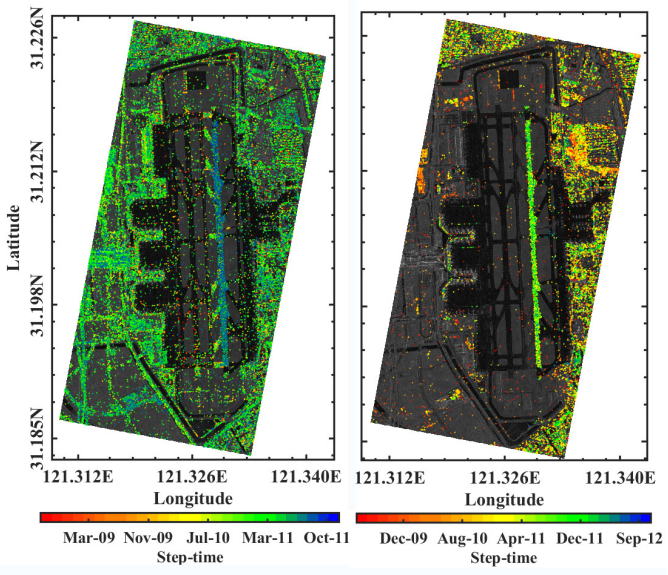

Fig. 18: Change detection in the construction area of Shanghai HongQiao airport. Left is appearance map and right is disappearance map.

D. Adaptive Temporal Subsets and Secondary Network

Four results considering the adaptive temporal subset approach and secondary network were obtained and only appearing TCS were used to perform a comparison. TABLE II shows the number of appearing TCS with different strategies. Fig. 19 shows the velocity of appearing TCS, where the number of appearing TCS is 62820.

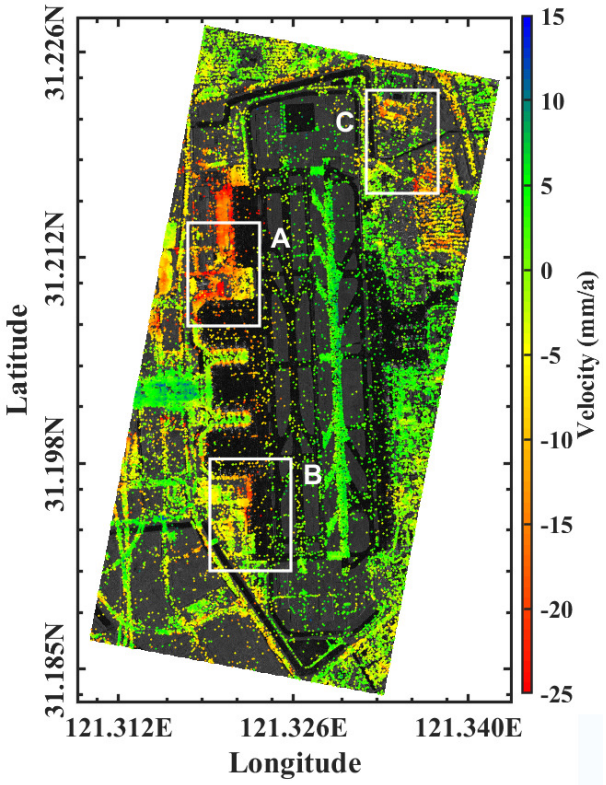

Fig. 19: Velocity of appearing TCS at HongQiao airport with a three-level (70/50/30%) process and a secondary network.

First, we used the three levels of temporal subsets, but did not apply the secondary network. The velocity of appearing TCS is shown in Fig. 20. The density of TCS is lower, and the total number of accepted TCS is much lower, i.e. 47119 points. Three small regions (A, B, and C) were selected to show more details, which were marked as three white rectangles in Figs. 19 and 20. According to Fig. 21, more TCS are accepted with the help of the secondary network, which shows details of the subsidence.

Second, the temporal subset approach was limited to only one level, i.e. 30% of the entire time series. However, this time, the secondary network was applied. Now, the number of accepted TCS is 63233, which contains a similar point density

The third test was applied with a one-level process (30% of the entire time range), but without the secondary network. The number of accepted TCS is 42672 and the point density over the runways is lower again, From the comparison, both the one-level (30%) and three-level (70, 50, and 30%) processes show a relatively high point density, and the secondary network appears to be necessary if the PS are not evenly distributed over the whole area.

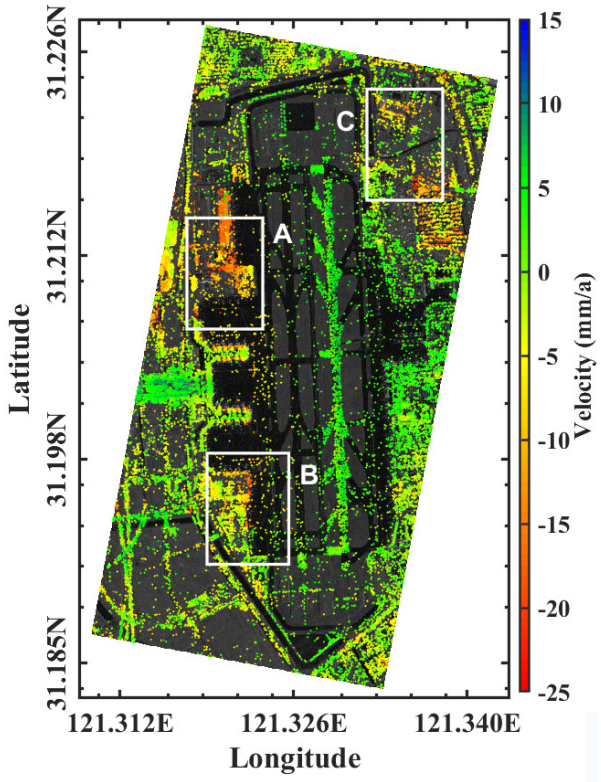

Fig. 20: Velocity of appearing TCS at HongQiao airport with a three-level (70/50/30%) process but without the secondary network.

TABLE II: Accepted number of appearing TCS with different strategies

	With secondary network	Without secondary network
Three levels	62820	47119
One level	63233	42672

The standard deviations (SDs) of the appearing TCS obtained by different strategies in the Shanghai case-study have been compared. The first comparison is the SDs of appearing TCS obtained by three-level and one-level with secondary network, which is shown in Fig. 22. The SDs of points obtained by the three-level process are smaller than those of points obtained by the one-level process. The quality of points with a longer time series is better than that of points with shorter time series, so its reasonable to process points with a different temporal support separately. The second comparison concerns the SDs of appearing TCS obtained by the three-levels approach with and without the secondary network, which is shown in Fig. 23. Although the number of points in these two groups is different, the SDs of the appearing TCS are similar. Through the above analysis considering the number of accepted TCS and their SDs, the process of the secondary network appears to be useful to include more potential TCS and the adaptive temporal subset approach is helpful to evaluate the quality of TCS properly.

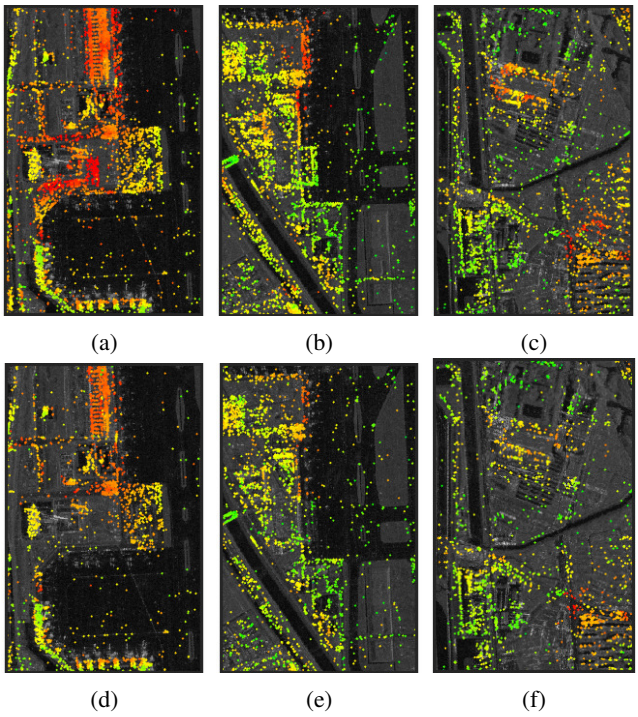

Fig. 21: Magnified views of selected area. The first row corresponds to velocity of appearing TCS with a secondary network, the second row to velocity of appearing TCS without a secondary network. (a) and (d) are region A. (b) and (e) are region B. (c) and (f) are region C. Colors are as in Fig. 19.

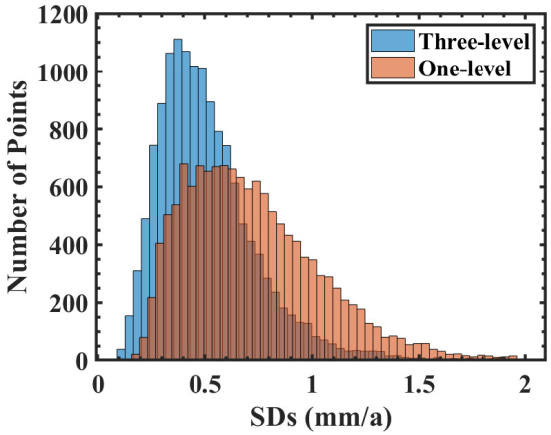

Fig. 22: Comparison of SDs on TCS obtained by the three-level (70/50/30%) and the one-level (30%) processing.

V. Conclusions

A new method for processing TCS is proposed based on amplitude change detection. Amplitude time series can be used to select potential TCS and locate the step-time automatically. Assuming a Rayleigh distribution, two hypothesis tests are introduced to conduct single pixel change detection. The interferometric phase is used to refine the initial result and estimate the parameters of the TCS. Only TCS which have enough arcs connected to the reference network are accepted, which separates the pure noise and true TCS from the candidates.

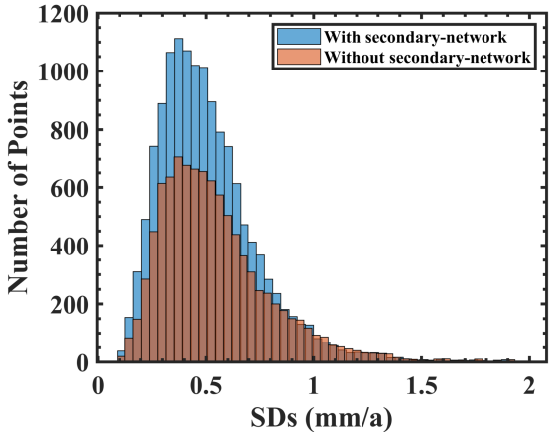

Fig. 23: Comparison of SDs on TCS obtained by the three-level (70/50/30%) process with and without the secondary network.

Additionally, during the interferometric processing of the TCS, an adaptive temporal subset approach is established, considering the length of the time series, to improve the precision of the estimates. A secondary network is used to include as many points as possible. Both options improve the density and precision of the final points especially for a spatially uneven distribution of points over the area. Two cases with a different distribution of points using S1A data in Delft and TSX data in Shanghai Hongqiao international airport were conducted. Not only does the velocity map of the TCS have a greater point density and show the deformation characteristics of the area, but it also highlights the changes in the construction area accurately.

Acknowledgment

Thanks to Copernicus Sentinel data 2017 and 2018, retrieved from ASF DAAC 8 March 2018, processed by ESA. Thanks to maps from GOOGLE EARTH PRO, DigitalGlobe 2018. (Oct 11, 2015 and Aug 27, 2016). Delft, the Netherlands. 52° N, 4°E. [March 2018]. And also thanks DLR service for offering TerraSAR-X images.

References

[1] R. F. Hanssen, *Radar Interferometry: Data Interpretation and Error Analysis*. Dordrecht: Kluwer Academic Publishers, 2001.

[2] H. A. Zebker, P. A. Rosen, and S. Hensley, "Atmospheric effects in interferometric synthetic aperture radar surface deformation and topographic maps," *Journal of Geophysical Research*, vol. 102, no. B4, pp. 7547–7563, Apr. 1997.

[3] J. Biggs, "InSAR observations of the earthquake cycle on the Denali fault, Alaska," Ph.D. dissertation, University of Oxford, 2007.

[4] P. Berardino, G. Fornaro, R. Lanari, and E. Sansosti, "A new algorithm for surface deformation monitoring based on small baseline differential SAR interferograms," *IEEE Transactions on Geoscience and Remote Sensing*, vol. 40, no. 11, pp. 2375–2383, 2002.

[5] P. He, Y. Wen, C. Xu, Y. Liu, and H. Fok, "New evidence for active tectonics at the boundary of the Kashi depression, China, from time series InSAR observations," *Tectonophysics*, vol. 653, pp. 140 – 148, 2015. [Online]. Available: http://www.sciencedirect.com/science/article/pii/S0040195115002280

[6] M. Born and E. Wolf, *Electromagnetic Theory of Propagation Interference and Diffraction of Light*. New York: Pergamon Press, 1980.

[7] J.-S. Lee, A. R. Miller, and K. W. Hoppel, "Statistics of phase difference and product magnitude of multi-look processed Gaussian signals," *Waves in Random Media*, vol. 4, no. 3, pp. 307–319, Jul. 1994.

[8] A. Ferretti, C. Prati, and F. Rocca, "Nonlinear subsidence rate estimation using permanent scatterers in differential SAR interferometry," *IEEE Transactions on Geoscience and Remote Sensing*, vol. 38, no. 5, pp. 2202–2212, Sep. 2000.

[9] ——, "Permanent scatterers in SAR interferometry," *IEEE Transactions on Geoscience and Remote Sensing*, vol. 39, no. 1, pp. 8–20, Jan. 2001.

[10] N. Adam, B. M. Kampes, and M. Eineder, "Development of a scientific persistent scatterer system: Modifications for mixed ERS/ENVISAT time series," in *ENVISAT & ERS Symposium, Salzburg, Austria, 6–10 September, 2004*, 2004, p. 9. [Online]. Available: http://doris.tudelft.nl/Literature/adam04.pdf

[11] J. Wu and F. Hu, "Monitoring ground subsidence along the Shanghai Maglev zone using TerraSAR-X images," *IEEE Geoscience and Remote Sensing Letters*, vol. 14, no. 1, pp. 117–121, 2017.

[12] D. Perissin and T. Wang, "Time-series InSAR applications over urban areas in China," *IEEE journal of selected topics in applied earth observations and remote sensing*, vol. 4, no. 1, pp. 92–100, 2011.

[13] U. Wegmuller, D. Walter, V. Spreckels, and C. L. Werner, "Nonuniform ground motion monitoring with TerraSAR-X persistent scatterer interferometry," *IEEE Transactions on Geoscience and Remote Sensing*, vol. 48, no. 2, pp. 895–904, 2010.

[14] H. Ansari, F. De Zan, and R. Bamler, "Sequential estimator: Toward efficient InSAR time series analysis," *IEEE Transactions on Geoscience and Remote Sensing*, vol. 55, no. 10, pp. 5637–5652, 2017.

[15] S. Samiei-Esfahany, J. E. Martins, F. van Leijen, and R. F. Hanssen, "Phase estimation for distributed scatterers in InSAR stacks using integer least squares estimation," *IEEE Transactions on Geoscience and Remote Sensing*, vol. 54, no. 10, pp. 5671–5687, 2016.

[16] O. Mora, J. J. Mallorqui, and A. Broquetas, "Linear and nonlinear terrain deformation maps from a reduced set of interferometric SAR images," *IEEE Transactions on Geoscience and Remote Sensing*, vol. 41, no. 10, pp. 2243–2253, 2003.

[17] A. Hooper, H. Zebker, P. Segall, and B. Kampes, "A new method for measuring deformation on volcanoes and other non-urban areas using InSAR persistent scatterers," *Geophysical Research Letters*, vol. 31, pp. L23 611, doi:10.1029/2004GL021 737, Dec. 2004.

[18] A. Hooper, P. Segall, and H. Zebker, "Persistent scatterer interferometric synthetic aperture radar for crustal deformation analysis, with application to Volcán Alcedo, Galápagos," *Journal of Geophysical Research: Solid Earth*, vol. 112, no. B7, 2007.

[19] P. Shanker and H. Zebker, "Persistent scatterer selection using maximum likelihood estimation," *Geophysical Research Letters*, vol. 34, no. 22, 2007.

[20] S. Navneet, J.-W. Kim, and Z. Lu, "A new InSAR Persistent Scatterer selection technique using top eigenvalue of coherence matrix," *IEEE Transactions on Geoscience and Remote Sensing*, vol. 56, no. 4, pp. 1969–1978, 2018.

[21] A. Ferretti, C. Colesanti, D. Perissin, C. Prati, and F. Rocca, "Evaluating the effect of the observation time on the distribution of SAR permanent scatterers," in *Third International Workshop on ERS SAR Interferometry, 'FRINGE03', Frascati, Italy, 1-5 Dec 2003*, 2003, pp. 1–5.

[22] D. Perissin and A. Ferretti, "Urban-target recognition by means of repeated spaceborne SAR images," *Geoscience and Remote Sensing, IEEE Transactions on*, vol. 45, no. 12, pp. 4043–4058, Dec 2007.

[23] L. Zhang, "Temporarily coherent point sar interferometry," Ph.D. dissertation, The Hong Kong Polytechnic University, 2012.

[24] L. Zhang, X. Ding, and Z. Lu, "Ground settlement monitoring based on temporarily coherent points between two SAR acquisitions," *ISPRS Journal of Photogrammetry and Remote Sensing*, vol. 66, no. 1, pp. 146–152, 2011.

[25] J.-S. Lee and E. Pottier, *Polarimetric radar imaging: from basics to applications*. CRC press, 2017.

[26] F. Bovolo, C. Marin, and L. Bruzzone, "A hierarchical approach to change detection in very high resolution SAR images for surveillance applications," *IEEE Transactions on Geoscience and Remote Sensing*, vol. 51, no. 4, pp. 2042–2054, 2013.

[27] O. Dogan and D. Perissin, "Detection of multitransition abrupt changes in multitemporal SAR images," *IEEE Journal of Selected Topics in Applied Earth Observations and Remote Sensing*, vol. 7, no. 8, pp. 3239–3247, 2014.

[28] J. L. Devore and K. N. Berk, *Modern mathematical statistics with applications*. Springer, 2012.

[29] T. Eltoft, "The Rician inverse Gaussian distribution: a new model for non-Rayleigh signal amplitude statistics," *IEEE Transactions on Image Processing*, vol. 14, no. 11, pp. 1722–1735, 2005.

[30] B. Kampes, *Displacement Parameter Estimation using Permanent Scatterer Interferometry*, Sep. 200.

[31] F. J. van Leijen, "Persistent scatterer interferometry based on geodetic estimation theory," Ph.D. dissertation, Delft University of Technology, Delft, the Netherlands, 2014.

[32] T. Li, G. Liu, H. Lin, H. Jia, R. Zhang, B. Yu, and Q. Luo, "A hierarchical multi-temporal InSAR method for increasing the spatial density of deformation measurements," *Remote Sensing*, vol. 6, no. 4, pp. 3349–3368, 2014.

[33] R. Bamler and P. Hartl, "Synthetic aperture radar interferometry," *Inverse Problems*, vol. 14, pp. R1–R54, 1998. [Online]. Available: http://doris.tudelft.nl/Literature/bamler98.pdf

[34] G. L. Stüber, *Principles of mobile communication*. Springer, 2017, vol. 2.

[35] M. Siddiqui, "Statistical inference for rayleigh distributions," *Journal of Research of the National Bureau of Standards, Sec. D*, vol. 68, no. 9, p. 1007, 1964.

[36] ——, "Some problems connected with Rayleigh distributions," *Journal of Research of the National Bureau of Standards*, vol. 66, no. 2, pp. 167–174, 1962.

[37] H. Cramér, *Mathematical methods of statistics (PMS-9)*. Princeton University Press, 2016, vol. 9.

[38] B. M. Kampes and R. F. Hanssen, "Ambiguity resolution for permanent scatterer interferometry," *IEEE Transactions on Geoscience and Remote Sensing*, vol. 42, no. 11, pp. 2446–2453, Nov. 2004. [Online]. Available: http://doris.tudelft.nl/Literature/kampes04.pdf

[39] F. Hu and J. Wu, "Improvement of the multi-temporal InSAR method using reliable arc solutions," *International Journal of Remote Sensing*, vol. 39, no. 10, pp. 3363–3385, 2018.

[40] P. J. G. Teunissen, "The least-squares ambiguity decorellation adjustment: a method for fast GPS integer ambiguity estimation," *Journal of Geodesy*, vol. 70, no. 1-2, pp. 65–82, 1995.

[41] S. Verhagen and P. J. Teunissen, "New global navigation satellite system ambiguity resolution method compared to existing approaches," *Journal of Guidance, Control, and Dynamics*, vol. 29, no. 4, pp. 981–991, 2006.

[42] S. Even, *Graph algorithms*. Cambridge University Press, 2011.

[43] A. Ataei, "Improved Qrginv algorithm for computing Moore-Penrose inverse matrices," *ISRN Applied Mathematics*, vol. 2014, 2014.

[44] D. Sandwell, R. Mellors, X. Tong, M. Wei, and P. Wessel, "GMTSAR: An InSAR processing system based on Generic Mapping Tools," 2011.

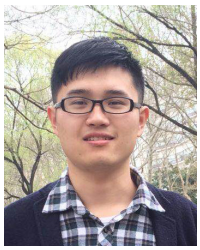

Fengming Hu received the B.E. degree in surveying engineering from Tongji University, Shanghai, China in 2014. He is currently working toward the Ph.D. degree with the College of Surveying and Geo-Informatics, Tongji University, Shanghai. During the period of October 2017 to October 2019, he was a guest Ph.D. student at the Delft University of Technology, the Netherlands

His interest includes deformation monitoring, 3-D model of the infrastructures, urban change detection and dynamic data processing using synthetic aperture radar images.

Jicang Wu received B.E. degree in Department of Geomatics from Wuhan Technical University of Surveying and Mapping in 1986, M.S.E. degree in Department of Surveying from Tongji University in 1989, and Ph.D. degree in Department of Land Surveying and Geo-Informatics from Hong Kong Polytechnic University in 1998.

He has been a professor in College of Surveying and Geo-Informatics with the Tongji University, Shanghai, China. He is specialized in crustal deformation montoring and inversion analysis.

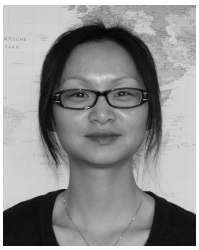

Ling Chang received the M.S.E. degree in geodesy and survey engineering from Tongji University, Shanghai, China, and the Ph.D. degree from the Delft University of Technology, Delft, The Netherlands, in 2010 and 2015, respectively.

Since 2018, she has been an Assistant Professor of microwave remote sensing with the ITC, University of Twente, Enschede, The Netherlands. Her current research interests include statistical hypothesis testing, time series modelling, and change detection, using satellite-borne remote sensing technology.

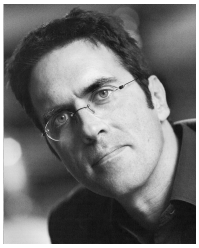

Ramon F. Hanssen (M'04-SM'15) received the M.Sc. degree in geodetic engineering and the Ph.D. degree (cum laude) from Delft University of Technology, The Netherlands, in 1993 and 2001, respectively.

He was with the International Institute for Aerospace Survey and Earth Science (ITC), Stuttgart University, Stuttgart, Germany; the German Aerospace Center (DLR), Weling, Germany; Stanford University, Stanford, CA, USA, as a Fulbright Fellow; and the Scripps Institution of Oceanography, University of California at San Diego, La Jolla, CA, USA, involved in microwave remote sensing, radar interferometry, signal processing, and geophysical application development. Since 2008, he has been an Antoni van Leeuwenhoek Professor in earth observation with the Delft University of Technology, where he has been leading the research group on mathematical geodesy and positioning since 2009. He has authored a textbook on radar interferometry.